# Finite Element Analysis of Fluid–Structure Interaction in a Model of an L-Type Mg Alloy Stent-Stenosed Coronary Artery System

**Yizhe Chen** [1,2,†], **Yuzhuo Yang** [1,3,†], **Hui Wang** [1,2], **Wenpeng Peng** [4,*], **Xunan Lu** [1,3], **Yijia Peng** [1,3], **Feng Zheng** [5] **and Shanshan Chen** [5,*]

1   Hubei Key Laboratory of Advanced Technology for Automotive Components,
    Wuhan University of Technology, Wuhan 430070, China; yzchen@whut.edu.cn (Y.C.);
    yzyang@whut.edu.cn (Y.Y.); huiwang@whut.edu.cn (H.W.); anxunlu@whut.edu.cn (X.L.);
    yjpeng@whut.edu.cn (Y.P.)
2   Hubei Engineering Research Center for Green & Precision Material Forming, Wuhan 430070, China
3   School of Automotive Engineering, Wuhan University of Technology, Wuhan 430070, China
4   Union Hospital, Tongji Medical College, Huazhong University of Science and Technology,
    Wuhan 430022, China
5   Institute of Metal Research, Chinese Academy of Sciences, Shenyang 110016, China; fzheng@imr.ac.cn
*   Correspondence: pengwenpeng@126.com (W.P.); sschen@imr.ac.cn (S.C.)
†   These authors contributed equally to this work and should be considered co-first authors.

**Abstract:** The coronary stent deployment and subsequent service process is a complex geometric/physical nonlinear and fluid–structure coupling system. Analyzing the distribution of stress–strain on the stent is of great significance in studying the deformation and failure behavior. A coupled system dynamics model comprising stenotic coronary artery vessels and L-type Mg alloy stents was established by applying the polynomial hyperelastic constitutive theory. The nonlinear, significant deformation behavior of the stent was systematically studied. The stress–strain distribution of the coupling system during stent deployment was analyzed. The simulation results show that the edges of the supporting body fixed without a bridge are the weakest zone. The stress changes on the inside of the wave of the supporting body are very large, and the residual stress accumulated in this area is the highest. The peak stress of the plaque and the arterial wall was lower than the damage threshold. The velocity of the blood between the wave crest of the supporting body is large and the streamline distribution is concentrated. In addition, the inner surface pressure on the stent is evenly distributed along its axial dimension. The maximum arterial wall shear stress always appears on the inside of the wave crest of the supporting body fixed with a bridge, and, as such, the largest obstacle to the blood flow is in this zone.

**Keywords:** L-type degradable magnesium alloy coronary artery stent; nonlinear finite element; fluid–structure interaction; distribution of stress and strain

## 1. Introduction

Interventional stent therapy is one of the methods used for the clinical treatment of coronary atherosclerosis. The principle of this method is that the stent is crimped onto a balloon and then deployed to the site of the arterial stenosis site; then, the balloon is inflated, thereby pushing the plaque onto the arterial wall, which, in turn, allows better flow of the blood through the artery [1,2]. Mg alloy coronary vascular stents are promising new vascular stents because of their excellent radial force, corrosion resistance, and in vivo degradability [3–5]. Clinical results indicate that dynamic mechanical effects, such as coupled vessel wall deformation, plaque, and blood hemodynamics, contribute significantly to the failure and restenotic processes of a stent after it is deployed. The expanding and compressing properties of the stent are even more critical and directly affect assembly efficiency

and clinical performance of the stent [6]. Consequently, an active area in biomechanics is the determination of the mechanical response of the coupling system at each stage after the deployment of the stent.

Simulation is an effective method for solving millimeter-scale biomechanical problems [7], and it has been extensively used to study the mechanical behavior of Mg alloy coronary stents. Gunet al. [8] numerically examined the shear stress in the wall of the vessel in a coronary artery stent coupling system under pulsatile flow and found that there was a minimum wall shear stress near the bridge and that wall shear stress was related to blood inlet velocity, with a positive correlation with acceleration. Wei et al. [9] designed and constructed a set of hemodynamic testing devices for coronary stent coupling systems. The results were in good agreement, validating the validity of the finite element analysis (FAE) method. Some works are concerned that the structure of coronary artery stents may affect their mechanical properties after the intervention. Jiang et al. [10] compared and analyzed the mechanical response of a coupling system after the deployment of S-type and N-type coronary stents in stenotic vessels. The results showed significant differences in the stress gradient on the vessel wall and on the plaque. Li et al. [11] determined the damage caused by different coronary artery stent types to blood vessels based on the impact of shear-thinning blood. According to the results, an N-type stent has a small wall shear stress area and a large cross-sectional area. Song et al. [12] ignored the plaque and simulated the mechanical properties of a V-type coronary artery stent after structural optimization. The results showed that adjusting the stent structure can improve its radial strength and bending flexibility. Using numerical simulation, Melzer et al. [13] examined the wall shear stress of vessel walls after the deployment of coronary stents with different structural arrangements. It was found that the type of bridge influences the safety of the coupled system. Numerous numerical simulations have been carried out on various coronary artery stents with various structures, and many conclusions have been reached. As coronary artery stent technology research has advanced, more excellent structures have become available. Ren et al. [14] simulated the flexibility of different L-, V-, and S-type coronary artery stents in the crimped state. The results showed that the radial recoil of L-type coronary stents was the smallest, and it was easiest to achieve the expected ideal shape after the intervention. Feng et al. [15] studied the fatigue performance of coronary artery stents in vascular pulsation using numerical simulation without considering the plaque. The results showed that an L-type coronary stent has a fatigue life of at least 10 years. These findings suggest that L-type coronary stents have excellent mechanical properties and good clinical potential. The structural safety and restenosis issues involving L-type coronary artery stents have received considerable research attention. Ross et al. [16] and Daniel et al. [17]. Used the FEA method to study the expansion performance of L-type coronary artery stents in a coupling system. Through a multi-objective optimization algorithm and filling nanomaterial technique, the stiffness and stability of coronary artery stents were improved after their deployment. Ahrens et al. [18] studied the distribution of wall shear stress on the vessel wall in the L-, O-, and S-type coronary artery stent coupling systems and found that the L-type stent has the smallest recirculation area and caused the least damage to the arterial vessel wall. A study by Claudio et al. [19] found that disturbances to blood after stent insertion, especially wall shear stress at the stent level, are also important factors that lead to stent thrombosis and restenosis. However, current studies focus on wall shear stress at the vessel wall or in the plaque [20–28], ignoring the research from the stent level. The related factors (i.e., the distribution of wall shear stress and pressure) caused by blood interference need further study. Because of the complex geometric/physical nonlinear deformation process of coronary artery stents, it is also of great significance to analyze the stress and strain distribution of stents. However, when discussing the expansion-contraction performance of stents in the above literature, the performance of stents during spring-back is often ignored, and the local dangerous points and their stress–strain history in the complete deformation stage of stents are not deeply studied, and the weak areas of materials on stents also need to be further evaluated. In this

paper, the motivation is to obtain the mechanical response of an L-type Mg alloy coronary artery stent in the process of deformation, predict the failure position of the stent, and reveal the rules of transient parameters related to restenosis at the stent level.

In order to study the stress–strain distribution at risk points and the laws of relevant fluid–structure coupling parameters on the L-type Mg alloy coronary artery stent during the complete deformation process, based on the theoretical notion of hyperelasticity, the dynamic model of the vascular coupling system of coronary stent deployment in stenosis was investigated. Additionally, the complex mechanical response of a stent in the process of large nonlinear deformation, the effect of stent deployment on the plaque and the vessel wall, and the transient variation of parameters related to restenosis at the stent level were also studied.

## 2. Materials and Methods

### 2.1. Material Properties

The L-type coronary stent was fabricated from a biodegradable Mg alloy (AZ31B) by laser cutting, with the mini-tube produced by EUROFLEX. The stent structure and its mechanical performance parameters were from the Institute of metals, Chinese Academy of Sciences. The stress–strain curve of the tube was drawn (Figure 1). Table 1 lists the mechanical properties of components.
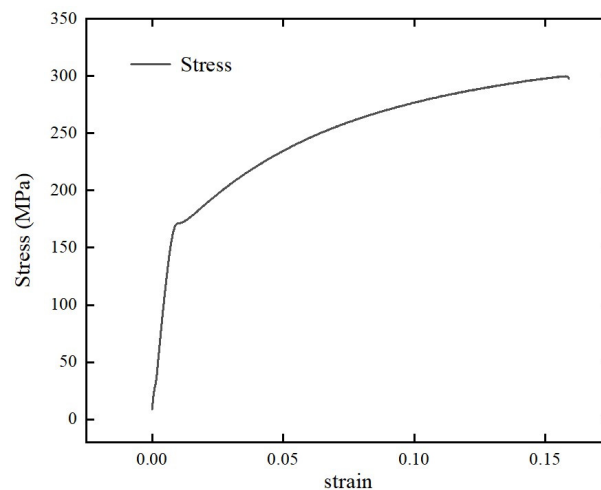
**Figure 1.** Tensile stress–strain curve for a Mg alloy (AZ31B).

**Table 1.** Mechanical properties of components.

| Components | Young's Modulus E (MPa) | Poisson's Ratio u |
|---|---|---|
| Stent | 44,800 | 0.35 |
| Balloon [16] | 300 | 0.30 |
| Crimper [16] | 300 | 0.30 |

The plaque and the vascular wall are incompressible hyperelastic materials. In order to improve the accuracy of simulation results, the reduction polynomial for the isotropic hyperelastic constitutive law was used to define material properties. The strain energy density formula is as follows [29]:

$$U = \sum_{i+j=1}^{N} C_{ij} (\bar{I}_1 - 3)^i (\bar{I}_2 - 3)^j + \sum_{i=1}^{N} \frac{1}{D_i} (J - 1)^{2i} \tag{1}$$

where $N$ represents the polynomial order and $D$ represents the compressibility of material. $D = 0$ indicates that the material is entirely incompressible, whereas $I1$ and $I2$ represent the

first and second strain tensors. If all $Cij = 0$ ($j \neq 0$), the constitutive model of the reduced polynomial can be derived as follows:

$$U = \sum_{i=1}^{N} C_{i0} \left(\bar{I}_1 - 3\right)^i + \sum_{i=1}^{N} \frac{1}{D_i} (J - 1)^{2i} \tag{2}$$

After consulting the literature [29], we took $N = 6$ and input the material parameters of the arterial and the plaque into the material library (Table 2).

**Table 2.** The diffusion coefficient of hydrogen in various elements.

| Parameter | C10 | C20 | C30 | C40 | C50 | C60 |
|---|---|---|---|---|---|---|
| Vessel Wall | 0.00625 | 0.04890 | −0.00926 | 0.76 | −0.43 | 0.08690 |
| Plaque | 0.00238 | 0.18900 | −0.38000 | 3.73 | −2.54 | 0.57300 |

### 2.2. Model and Mesh

First, we drew the plane unfolding graph of the stent using Autocad (2020, Autodesk, San Rafael, CA, USA) and then imported it into SolidWorks (2020, Dassault Systemes, Waltham, MA, USA) to obtain the 3D model of the stent by wrapping, suturing, mirroring, and deleting surfaces (Figure 2). The inner diameter of the stent was 2.12 mm, and the length of a single section was 3 mm. The bridge was an L-type, and the bridge width was 0.12 mm. The supporting body was symmetrically distributed in the circumferential direction, and there were six in total. The thickness of each supporting body was 0.14 mm.
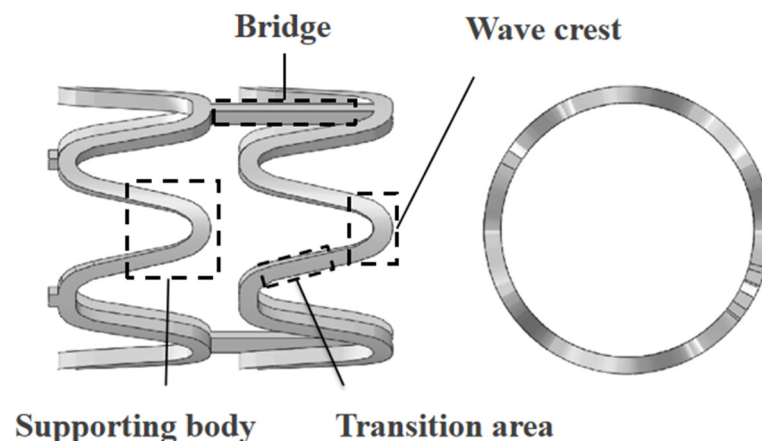
**Figure 2.** 3D model of Biotech's L-type coronary artery stent.

The vascular wall, plaque, crimper, and balloon were modeled in ABAQUS/Standard (2020, Dassault, France). The vessel wall and plaque were simplified as hollow cylinders. The crimper and the balloon were simplified as round shells. The extent of the initial stenosis rate was set at 40%, and the specific dimensions are given in Table 3. The "mesh" module of ABAQUS completed the meshing of the artery, plaque, crimper, balloon, and stent. The stent was irregular in shape and underwent significant deformation during its deployment, so 10-node tetrahedral elements (C3D10) were employed. The arterial wall and the plaque were taken to be isotropic hyperelastic materials. The 8-node linear hexahedron element (C3D8H) was used to mesh them. The artery wall was composed of the adventitia, the media, and the intima, so the thickness direction was divided into three layers of mesh approximation. The crimper and the balloon are similar in terms of material properties and structure. A 4-node curved shell (S4R) was used for mesh division. An integrated assembly is shown in Figure 3.

**Table 3.** Original dimensions for other geometric models (mm).

| Structure/Component | Inner Diameter | External Diameter | Length |
| --- | --- | --- | --- |
| Arterial Vessel | 3.2 | 3.6 | 9.0 |
| Plaque | 2.5 | 3.2 | 3.5 |
| Crimper | 2.6 | – | 5.0 |
| Balloon | 1.0 | – | 5.0 |
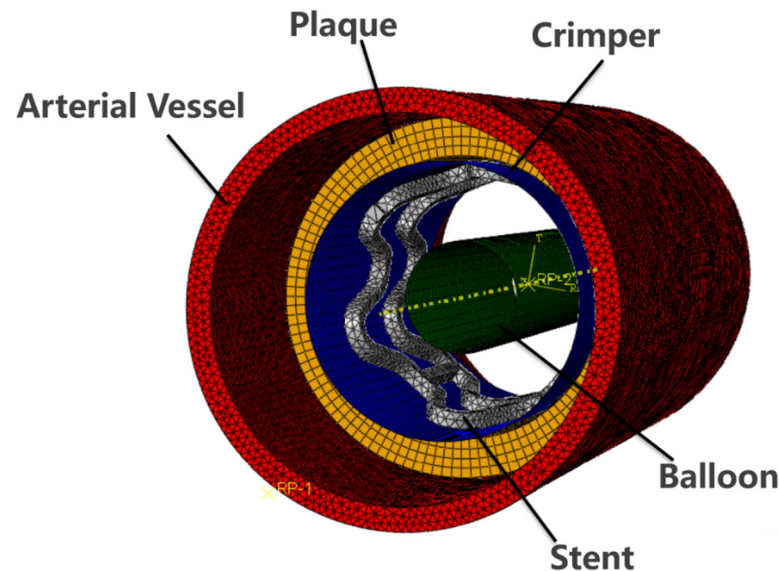
**Figure 3.** The mesh of L-type coronary artery stent coupling system.

### 2.3. Boundary and Load

The entire system should be constrained to avoid rigid body motion during the expansion and compression simulation. Using the cylindrical coordinate system, the outer wall of the plaque was rigid-bound to the inner wall of the vessel, and only the degree of freedom radial movement of the plaque was retained (U2 = U3 = UR1 = UR2 = UR3 = 0). Moreover, to keep the center of the system stable and not offset throughout the simulation process, it was necessary to "rigid-body-bind" point RP-1 on the axis to any point RP-2 outside the system and restrict all the freedom of the RP-2 point degree (U1 = U2 = U3 = UR1 = UR2 = UR3). The general static analysis used the quasi-Newton calculation criterion and initiated a nonlinear mode.

The stent must be loaded after the deployment to achieve expansion and compression by controlling the size of the balloon and the crimper. Therefore, to more accurately reflect the distribution of stress and strain on the stent, the displacement loading method should define the load applied to the balloon and the crimper. During the expansion process, the radial displacement of the balloon (U1) was equal to 0.90 mm to simulate the standard service outer diameter of 3.0 mm after stent expansion. When the stent was crimped, the radial displacement of the crimper (U1) was equal to 0.82 mm, and then the crimper was placed into the delivery system to simulate the actual crimping of the stent to an outer diameter of ≤1 mm and transported to the area of arteriosclerotic blockage. In addition, to investigate the spring-back phenomenon of the stent after plastic deformation, the load was removed quickly at the end of loading to simulate the whole deployment process of spring-back. Figure 4 shows the displacement loading process of the stents in the FAE.
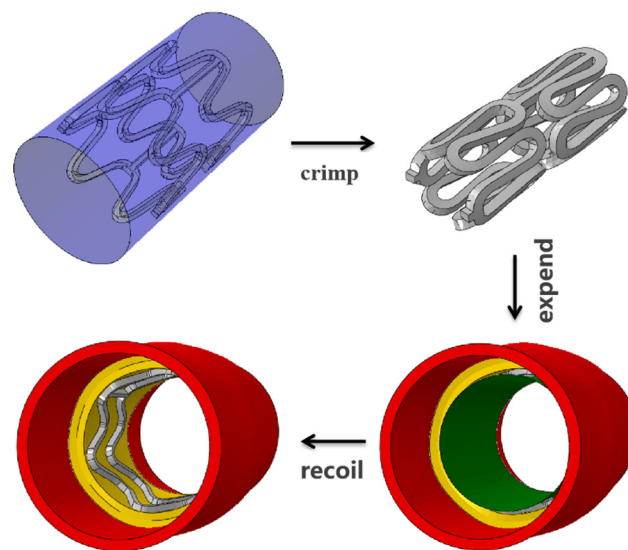
**Figure 4.** The displacement loading process of a coronary artery stent.

*2.4. Fluid –Stent Interaction Settings*

We implemented an analysis of the blood hemodynamics using Workbench (2021R1, ANASY, Canonsburg, PA, USA) computational fluid dynamics (CFD), focusing on blood flow effects on the stent. We developed a one-way fluid–structure coupling analysis model, including blood flow, the arterial vessel wall, and the stent after deployment. The blood flow area was determined by removing the stent volume from the cylinder enclosed by the vessel's inner diameter, as shown in Figure 5. Based on the physiological state of coronary artery vessels and the actual blood parameters, the blood inlet velocity, dynamic viscosity, and blood density were set to 0.12 m/s, 3.572 mPa·s, and 1100 kg/m$^3$, respectively. The essence of blood is an incompressible non-Newtonian fluid. However, in numerical simulation studies, the blood flow in large blood vessels such as the aorta is usually regarded as a Newtonian fluid, ignoring the viscoelasticity of the blood, and the viscosity is taken as the blood viscosity under the limit of the high shear rate, which helps to efficiently study and analyze the rheological properties of blood in complex calculation areas [30–32]. There is no slip along the wall, and the axial span is small. The relative pressure at the outlet was not set.
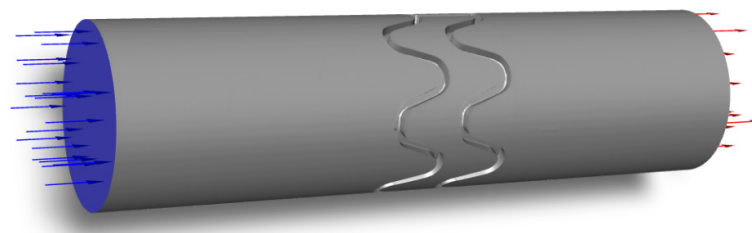
**Figure 5.** Finite element model of blood flow in the CFD module.

## 3. Results and Discussion

*3.1. Analysis of Stent Compression Performance*

Figure 6 shows the von Mises stress and maximum principal strain distribution at the crimp end. The stress level of the wave crest of the supporting body is the highest, followed by the transition area, the bridge area is the lowest, and the mean strain on the supporting body exceeds 0.08. Mutual extrusion occurred outside the wave crest of the supporting body when the stent was compressed to the minimum, and there were points on the stent with a wide range of stress exceeding 200 MPa. The high stress appears on the outside of the supporting body and the inside of the wave crest of the supporting body fixed without a bridge, and the maximum stress is 297.9 MPa. Additionally, large plastic

deformation occurred inside the wave crest with a maximum strain of 0.19. Therefore, the stress and strain are the direct basis for judging the failure behavior of the support. At the end of crimping, the stent may be partially ruptured, and the inside of the wave crest of the supporting body fixed without bridge is the most vulnerable area of material weakness. When the crimper was removed, the stent experienced severe radial recoil. Its outer diameter increased from 0.964 mm to 1.152 mm, and the parts that came in contact separated. The formula for calculating the radial compression recoil is as follows:

$$\alpha = (d1 - d2)/d2 \tag{3}$$

where d1 is the outer diameter of the recoil, d2 is the outer diameter of the end of crimping, and the calculated radial compression recoil is 19.3%, indicating that the stent has poor adhesion to the balloon. The distribution of the von Mises stress and the maximum principal strain after spring-back is depicted in Figure 7. The value and distribution of the maximum principal strain before and after spring-back remain unchanged. It is worth noting that the peak stress on the outside of the wave crest of the supporting body decreased from 250.5 MPa to 200.6 MPa, a decrease of 19.9%. The peak stress on the transition area decreased from 179.5 MPa to 79.1 MPa, which decreased by 55.7%. Figure 8 shows the stress–strain history of the weak point of the material and the transition region of the supporting body. It can be seen that the overall stress level of the supporting body dropped sharply at the moment of spring-back, whereas the strain level remained constant throughout the whole process. In the late recoil stage, the peak stress on the inside of the supporting body increased rapidly. This is due to the severe plastic deformation on the inside of the wave crest of the supporting body, and a large amount of residual stress will form after the stress is redistributed. In the whole compressing deformation stage, the peak stress and strain on the stent always appeared on the inside of the wave crest of the supporting body fixed without a bridge. The local deformation in this area was huge, and the point where the stress and strain were high was still retained after spring-back. Therefore, fracture of the stent during deployment cannot be avoided.
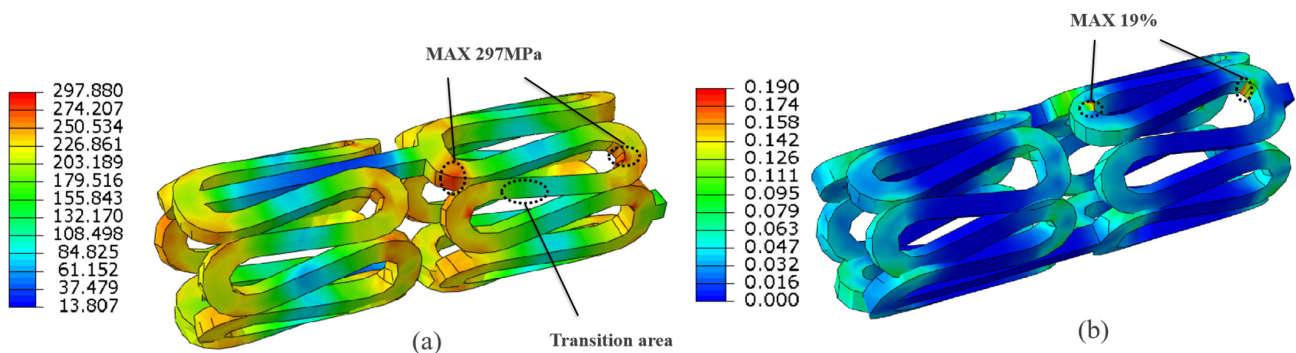
**Figure 6.** The equivalent stress (**a**) and equivalent strain (**b**) distribution clouds for the stent after crimping.

### 3.2. Evaluation of Stent Expansion Performance

Figure 9 shows the distributions of the von Mises stress and the maximum principal strain at the end of stent expansion. Figure 10 shows the von Mises stress and the maximum principal strain after balloon withdrawal and the stent spring-back. It can be seen from the stress distribution contours that after the stent expansion, the stress level on the supporting body is relatively high, ranging from 120.2 MPa to 209.1 MPa. The area of high stress was located on the outside of the wave crest of the supporting body fixed without a bridge, and it had a maximum stress value of 357.2 MPa. Taking this as an evaluation index of failure, there is also a risk of damage during the expansion process. It is predicted that this area is the weakest point in the stent. The mean strain of the wave crest of the supporting body is much higher than in other regions, and the strain on the connecting body is zero.

In contrast, the maximum strain (6.88%) was experienced on both insides of the wave crest of the supporting body fixed bridge. It shows that the combined bending and torsional deformation caused by the adjacent supporting elements' radial movement and expansion movement is assumed here, and the peak strain value is lower than the limit strain of the Mg alloy. Radial expansion recoil is an important parameter indicating the possible expansion of coronary stents in vivo. Radial expansion recoil was calculated as follows:

$$\beta = (D1 - D2) / D2 \qquad (4)$$

where D1 is the outer diameter at the end of the expansion and D2 is the outer diameter after spring-back, the actual diameter of the stent after expansion is 3.106 mm, and it is reduced to 2.937 mm after spring-back. The radial expansion of the stent was calculated to be approximately 5.4%. The overall stress level of the stent is significantly reduced after spring-back, and the change in strain is stable, indicating that the plaque is stably supported by the stent. At the end of the recoil stage, the peak stress level on the inside of the supporting body of stent also increased rapidly, the local high-stress points on the inside were retained, and the maximum stress was 337 MPa, which posed a risk of failure. Figure 11 shows the stress–strain history of the weak points in the stent and in the transition region of the supporting body during the expansion stage. The strain value of the outside of the wave crest of the supporting body and the transition zone is obviously lower than that of the inside of the wave crest of the supporting body, and the residual stress is relatively small, so their stress level decreases continuously in the recoil zone. Chen et al. [33] implanted a similar stent into the porcine coronary artery according to the nominal size and found that a stent with an outer diameter of 3 mm had a radial expansion recoil of approximately 4%. Then, the evolution of structural integrity after stent deployment was observed by high-resolution transmission X-ray tomography. The results showed that after 1 month in vivo, apparently, the stent had cracks on the outside of the supporting body fixed without a bridge (Figure 12a). Additionally, the cracks were found on the inside of the supporting body fixed with a bridge, and the cracks gradually expanded over the next 3 months in vivo, resulting in the final fracture (Figure 12b). In addition, at large strains, twinning and grain refinement were observed in the stent. It is speculated that the reason for the failure may be related to the stress concentration. The present FEA is consistent with the above-referenced in vivo results, thereby validating the coupling system dynamic model used in the present work.
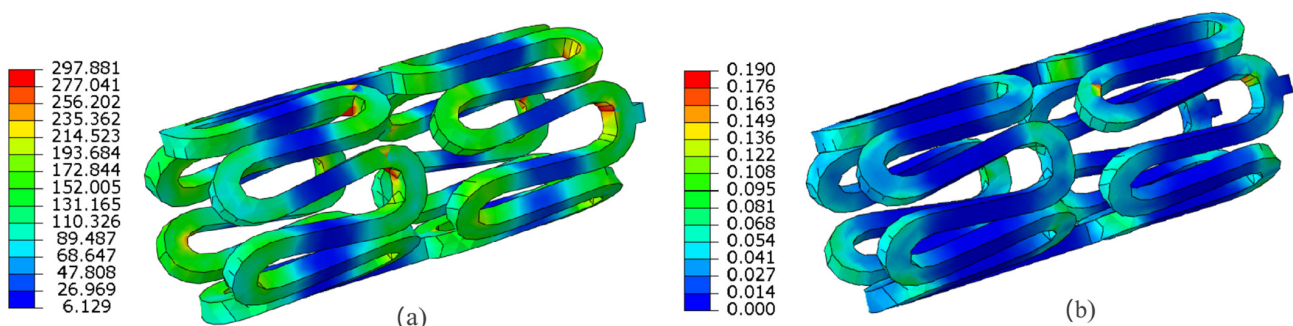
**Figure 7.** The equivalent stress (**a**) and equivalent strain (**b**) distribution contours for the stent after spring-back.
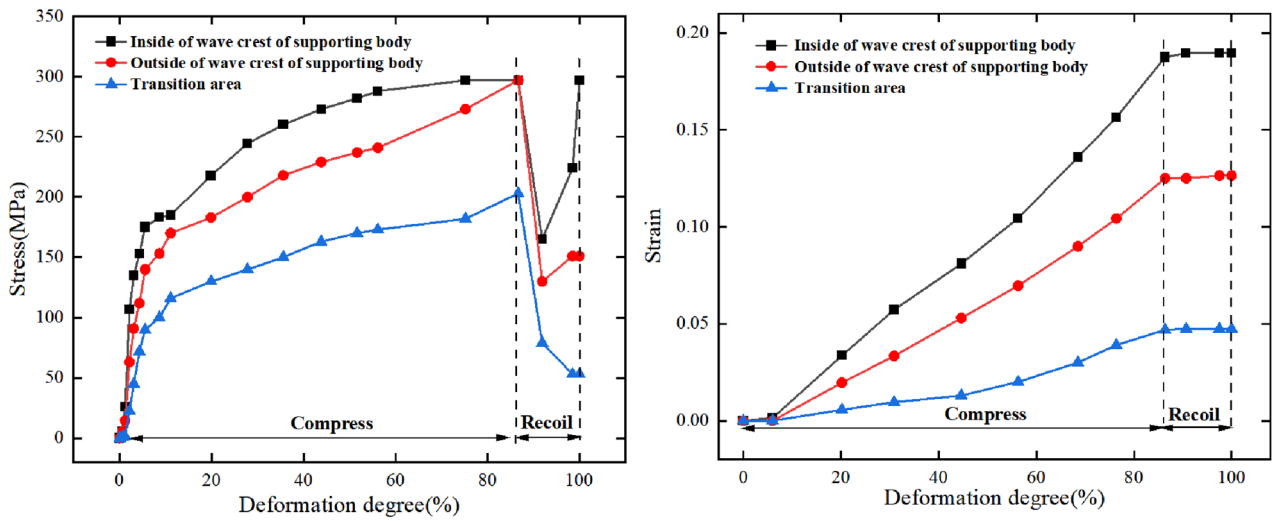
**Figure 8.** Variation of stress and strain at some points of L-type coronary stent during compression stage.
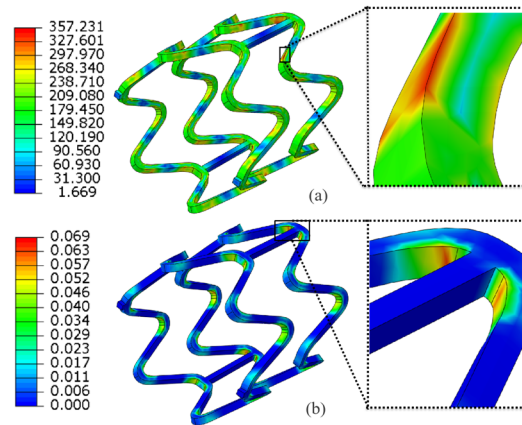
**Figure 9.** The equivalent stress (**a**) and equivalent strain (**b**) distribution of stent at the end of expansion.
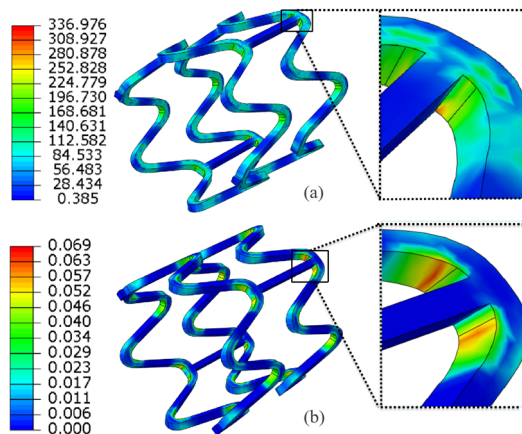
**Figure 10.** The equivalent stress (**a**) and equivalent strain (**b**) distribution of the stent after spring-back.
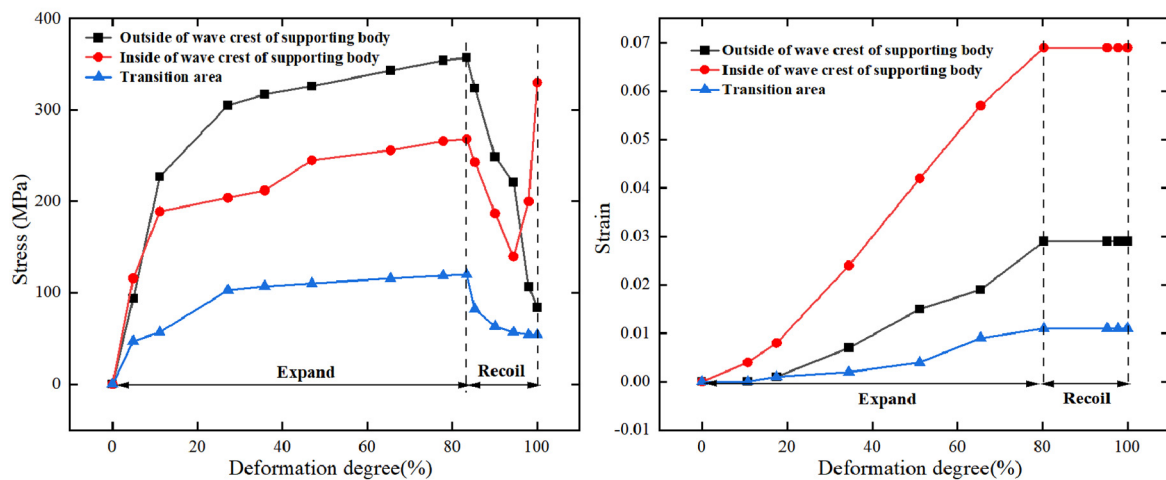
**Figure 11.** Variation of stress and strain at some points of L-type coronary stent during expansion stage.
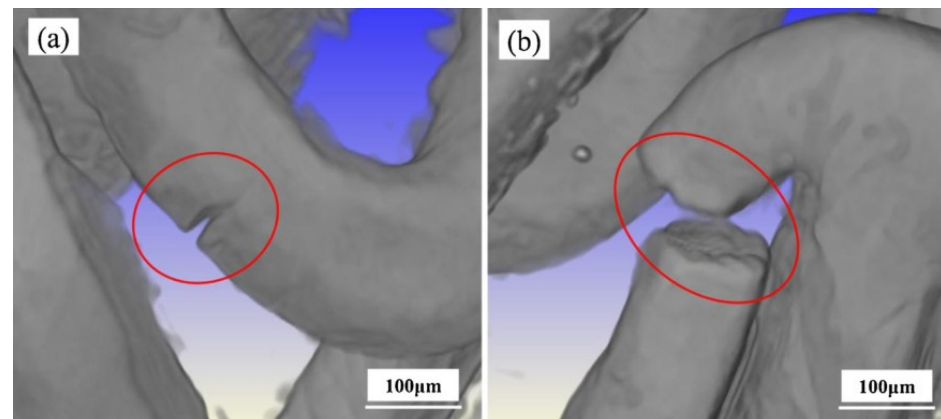
**Figure 12.** Failure behavior of the L-type AZ31B magnesium alloy coronary artery stent after 1 month (**a**) and 3 months (**b**) implantation. Reproduced with permission from [33], Copyright 2020 Elsevier.

### 3.3. Stress Analysis of Diseased Plaques and Vessel Walls

Figure 13 shows the von Mises stress, displacement distribution contours, and the von Mises stress distribution in the arterial vessel wall at the end of expansion. A large area of the stent (surgical area) is under compressive stress. The stress level at the location where the plaque is in contact with the stent supporting body is higher than in other parts. The maximum stress was 257.8 kPa, which is less than the most widely used damage threshold for plaque (300 kPa) [34] (the plaque approaching this threshold will directly rupture and cause fatal myocardial infarction). It is consistent with the experimental results proposed by Kamm et al. [34] that the maximum stress in a stable plaque is 193 ± 65 kPa. In addition, the stress from the inner surface to the outer surface of the plaque decreases gradually along the thickness direction, and the stress gradient is not equal, indicating that the expansion of the stent has different levels of high-stress stimulation to the cells of each layer of the arterial vessel wall. Additionally, the above high-stress area corresponds to the dark red concave area in the displacement contour. The plaque is essentially an incompressible severe calcification with a hard texture. Under the alternating load caused by the high-pressure stress, there is significant deformation and vascular radial pulsation (160 mmHg), which may culminate in the fatigue of the plaque. Therefore, the plaque may be much less than critical local fragility ruptures without warning under stress, resulting in intravascular restenosis. The stent transmits significantly lower stress on an arterial vessel wall than on the plaque. The stress in the section of the arterial wall in contact with the edge of the plaque is the largest (44.98 kPa) and the stress in the area near the supporting

body of the stent is between about 15 and 30 kPa. After the stent is deployed, the most vulnerable part of a coronary artery is the intima, and its failure stress is approximately 1300 kPa [35]. Therefore, under the condition that the stent does not warp, does not directly contact the blood vessel wall, and the deformation amount is accurately controlled, the stress on the blood vessel wall is predicted to be at a safe level. The stress distribution is depicted in Figure 14. It can be seen that, after an L-type coronary stent is deployed, there is a mismatch in the stress distribution on the plaque compared to that in the vessel wall.
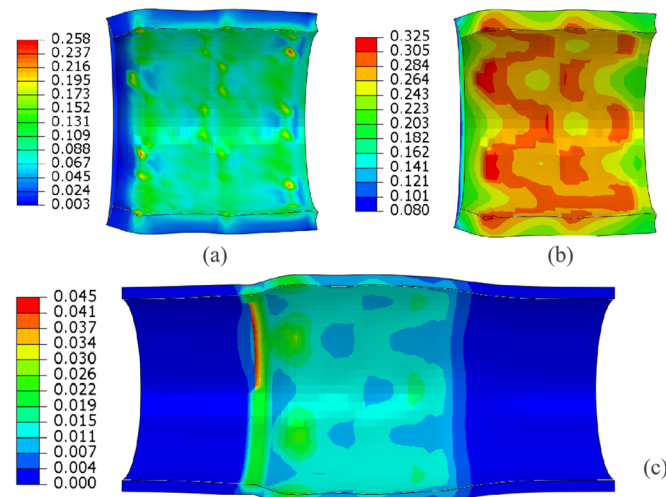
**Figure 13.** Distribution of equivalent stress (**a**), displacement (**b**), and equivalent stress (**c**) along the arterial wall after expansion of the stent.
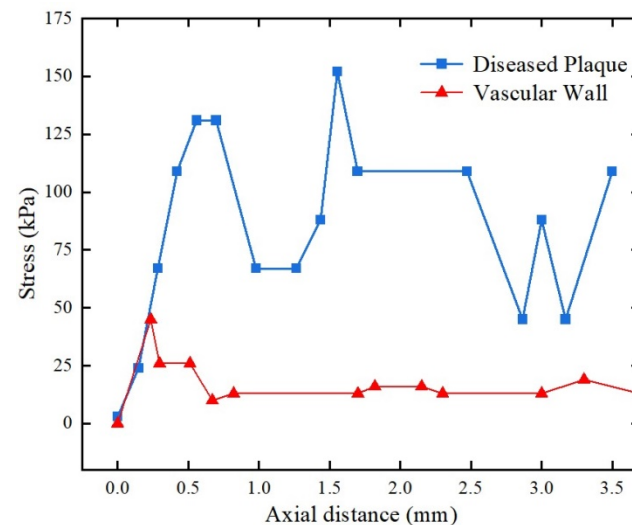
**Figure 14.** Distribution of stress along the axes of plaque and artery vessel wall.

*3.4. Blood Flow Distribution in Stents*

Under the influence of using a 3D model of a vascular coronary stent, the distribution of the blood velocity in the vessel was obtained (Figure 15). When a stable flow rate is applied at the inlet, the blood flow in the vessel is laminar, the blood flow rate along the axis of the arterial vessel is the largest, and the flow field distribution conforms to Poiseuille's law. When a stent is inserted, the blood around the stent is stagnant. The excessive thickness of the flowing boundary layer on the inner surface of the stent reduces the cross-sectional area where blood can flow and increases the central axial velocity rapidly. The peak flow velocity was 0.171 m/s, a 29.8% increase. The slow blood flow velocity inside the adherent wall is the primary factor leading to thrombosis. In addition, the blood flow velocity and the streamlines are denser in the gaps between the wave peaks of the adjacent supporting

body in the axial direction of the stent, which appear as local jumps in the blood flow field distribution contour, and then converge on the wave crest of the downstream supporting body. The tangential speed will be faster. Michal et al. [36,37] implanted a coronary artery stent with a standard outer diameter of 3.2 mm into an artificial stenotic vessel (stenosis extent = 55%) and measured the blood flow velocity at different positions in the vessel experimentally by a laser beam. The results show that blood arching could be observed around the wave crest of the supporting body, The central axis flow rate in the area covered by the stent was significantly higher than in other areas (Figure 16). The present FAE results are consistent with the results reported in the above-referenced in vivo study, which, again, validates the model of the coupled system dynamics used in the present study.
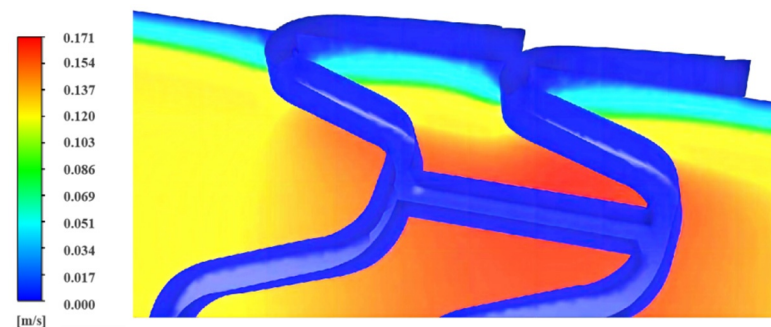
**Figure 15.** Intravascular flow field after coronary artery stent deployment.
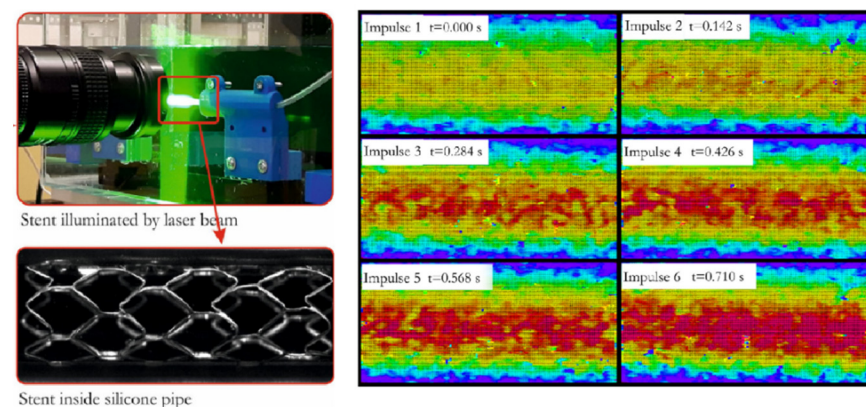
**Figure 16.** Blood velocity distribution in the vessel after coronary stent implantation Reproduced with permission from [37], Copyright 2020 Elsevier.

### 3.5. Law of Distribution of Pressure and Wall Shear Stress in Coronary Stents

After stent deployment, most biological reactions occur on the surface of the stent, and endothelial cells grow well on the surface of the stent, which is one of the effective schemes to prevent thrombosis. As a result of the pressure generated by the blood on the stent wall, the endothelial cells in the vessel wall are directly affected. Figure 17 depicts the contour of the pressure distribution of blood flowing against the stent. Sudden changes of pressure distribution along the axial direction may damage the intimal cells and cause inflammation. The maximum pressure (red area; 25.99 Pa) is evenly distributed on the upstream side of the supporting body. The pressure outside the supporting body gradually declines downhill in an axial direction and gradually increases radially outward along the arterial vessel wall. The mean pressure on the blood outlet side is significantly lower than that on the upstream side, with a peak pressure difference of 31.72%. As the inner surface of the stent is evenly distributed along the axial direction, there are no significant pressure fluctuations between upstream and downstream. Thus, it is predicted that the periodic flow of blood will not cause significant damage to the endothelial cells on the vessel wall after stent deployment since these cells are in a relatively stable physiological environment.
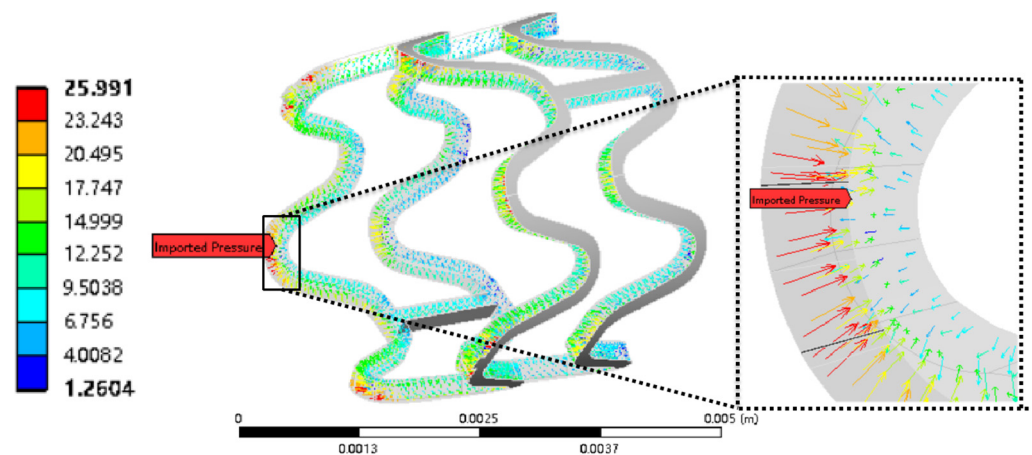
**Figure 17.** Pressure distribution of blood acting on the coronary artery stent at the maximum moment.

The wall shear stress of a stent reflects the frictional force on the blood flow and is used as a reference index for the design of stent surface texture (to reduce stagnation of stent). Figure 18 is the wall shear stress distribution on the stent at different times. Wall shear stress of the stent increases with time (Figure 19). From the moment the blood and the stent come into contact, the maximum shear stress increased from 2146.8 Pa to 10734 Pa, and the mean shear stress increased from 292.2 Pa to 1461 Pa, and the minimum shear stress increased from 1.45 Pa to 7.23 Pa. The shear stress on the stent varies dramatically over the cycle and is unequally distributed throughout the stent. The maximum wall shear stress always occurs on the inside of the wave crest of the supporting body fixed without the bridge, and the minimum wall shear stress always appears in the transition and bridge areas. This shows a high blood flow velocity gradient in the area near the inside of the wave crest of the supporting body fixed without a bridge, and this area is the most seriously obstructive to blood flow. Future work should focus on the surface texture design of the stent, optimizing the size of the supporting body, and setting a streamlined transition arc in the turbulence area to minimize the disturbance caused by the stent.
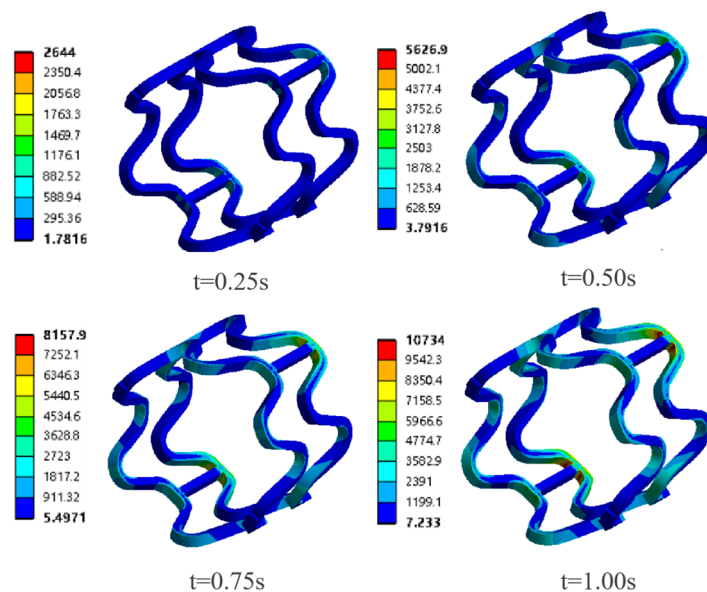
**Figure 18.** Distribution of wall shear stress (Pa) on the stent at different times.
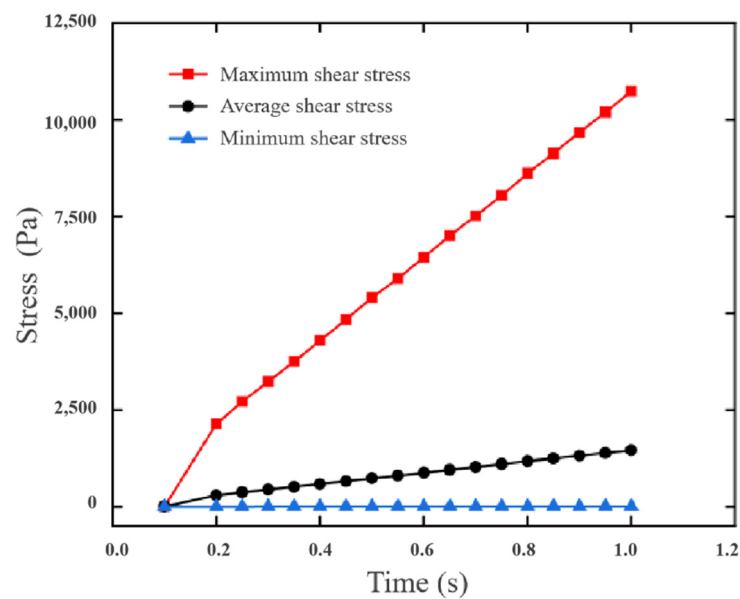
**Figure 19.** Variation of wall shear stress on the stent, with time, in a single cycle.

### 3.6. Verification of Computational Fluid Dynamics Results

To verify the accuracy of the above fluid–structure interactions, the inner wall of the stent is taken as the research object. The blood flow has been in complete contact with the stent at a particular time. Assuming that any point on the inner wall of the bridge area at that time is point 1 and on the blood flow axis is point 2, according to the Bernoulli flow mode, the following relationship exists between points 1 and 2:

$$\Delta P / \rho \cdot g = \Delta Z + \left( V1^2 / 2g - V2^2 / 2g \right) \tag{5}$$

where $\Delta P$, $\Delta Z$, $V$, $\rho$, and $g$ are the relative pressure difference, relative distance, blood flow velocity, blood density, and gravitational acceleration at point 1 and point 2, respectively. The theoretical wall shear stress of laminar flow in a circular pipe with diameter D was calculated, thus:

$$\tau = (\Delta P \times D) / 4 \cdot \Delta Z \tag{6}$$

Simultaneously for Equations (5) and (6), Z = 1.05 mm (inner radius of the stent); according to the FAE results, P1 = 0.12 m/s; P2 = 0.6 m/s; D is the inner diameter of stent = 2.1 mm; g is the local acceleration of gravity = 9.8 m/s$^2$; and blood density = 1100 kg/m$^3$. The results show that the theoretical value of the shear stress on the inner surface of the bridge area is 8.63 Pa under the condition that the blood flow is stable. This is different from the minimum shear stress of 7.23 Pa when the blood and the stent are in complete contact (t = 1 s), which verifies the rationality of the numerical simulation results.

### 3.7. Limitations of the Study

Theoretically, the whole deformation stage of the stent should be in the fluid flow and scouring environment, which can approach the real mechanical response of the stent deformation process. The simplified treatment (Ignore the role of blood) was considered to analyze the stress-strain history of compression and expansion performance of the stent, which is a limitation of this study. However, this treatment has little effect on the results of the stress–strain distribution on the stent and does not directly change the research conclusions. Compared with the external loads such as arterial vessels, plaque, and the balloon, which act on the stent and cause significant plastic deformation, the external force exerted by blood on the stent is rather weak, which can testify, using the simulation results, that the values of the former and latter are different by multiple orders of magnitude.

Another limitation in this study is that the boundary of the fluid is assumed to be a standard cylinder, and the blood flow velocity is considered stable. The true arterial vessel was locally curved, not an ideal straight line, and there was a certain fluctuation in the inlet flow rate. However, the research object in this paper is taken from a unit subsection on a complete coronary artery stent, whose axial size is very small, and most single subsections can assume that the arterial vessel is straight in the axial direction in which it is located. The variation of inlet and outlet blood flow velocity is small. Therefore, the flow field, pressure, and shear stress distributions obtained in this study at the level of blood flow acting on the stent are representative and can be applied to most areas of the stent.

## 4. Conclusions

The numerical simulation of a Mg alloy coronary artery stent intervention coupling system was modeled and analyzed. The results were used to determine the deformation and the influence of fluid during the large elastic-plastic deformation of the stent. The conclusions are as follows:

1.  The radial recoil in the compression stage is 19.3%. The inside of the wave crest of the supporting body fixed without a bridge is extensively compressed, the maximum stress is 298 MPa, and the maximum strain is 19%, which may cause fracture during the loading process. The local high-stress points inside the wave crest of the supporting body are still retained after spring-back.
2.  The radial recoil in the expansion stage is 5.4%. At the outside of the wave crest of the supporting body fixed without a bridge, the stress is high at 357 MPa, which increases the risk of causing local cracking. The maximum strain is 6.9%, located at the inside of the wave crest of the supporting body fixed with a bridge, and a combined bending and torsion deformation occurs in this region.
3.  The maximum stresses in the plaque and the vascular wall are 258 kPa and 45 kPa, respectively, which are lower than the damage threshold, but the plaque is at risk of fatigue in the long term.
4.  Stagnation occurs around the stent. The velocity of the blood between the wave crest of the supporting body is large and the streamline distribution is concentrated. The maximum blood flow pressure (26 Pa) is located on the upstream side of the wave crest of the supporting body. The pressure on the inner wall of the stent is evenly distributed along the axis, and the environment of the endothelial cells is stable.
5.  The maximum shear stress (approximately 11 kPa) is always on the inside of the wave crest of the supporting body fixed with a bridge, and the blood flow velocity gradient in this area is the largest.

**Author Contributions:** Conceptualization, W.P. and S.C.; methodology, Y.C. and Y.Y.; data curation, Y.Y.; writing—original draft preparation, Y.C. and Y.Y.; writing—review and editing, S.C. and F.Z.; funding acquisition, Y.C. and Y.Y.; project administration, Y.C. and H.W.; investigation, X.L. and Y.P. All authors have read and agreed to the published version of the manuscript.

**Funding:** This work was supported by the National Natural Science Foundation of China (Grant No. 52175360, 51901227), the Young Elite Scientists Spxonsorship Program by CAST (Grant No. 2021QNRC001), the China Postdoctoral Science Foundation (2022M710062), the National innovation and entrepreneurship training program for college students (Grant No. 3120400002356), and "the Fundamental Research Funds for the Central Universities" (Grant No. 2020III004XZ).

**Institutional Review Board Statement:** Not applicable.

**Informed Consent Statement:** Not applicable.

**Data Availability Statement:** Data are contained within the article and can be requested from the corresponding author.

**Acknowledgments:** Special thanks to the National College Student Innovation and Entrepreneurship Training Program (Grant No. 3120400002356) for supporting this research.

**Conflicts of Interest:** The authors declare no conflict of interest.

## References

1.  Bailey, S.R. Next-Generation Coronary Stents: Thin Is In; Subacute Thrombosis Is Where It Is At; Restenosis Is Not Hopeless. *JACC Cardiovasc. Interv.* **2020**, *13*, 831–832. [CrossRef]
2.  Kereiakes, D.J.; Kandzari, D.E.; Zidar, J.P. Drug-Coated Balloons for In-Stent Restenosis. *J. Am. Coll. Cardiol.* **2020**, *76*, 1391–1392. [CrossRef]
3.  Gori, T. Vascular Wall Reactions to Coronary Stents—Clinical Implications for Stent Failure. *Life* **2021**, *11*, 63. [CrossRef]
4.  Bao, G.; Fan, Q.; Ge, D.; Sun, M.; Guo, H.; Xia, D.; Liu, Y.; Liu, J.; Wu, S.; He, B.; et al. In vitro and in vivo studies on magnesium alloys to evaluate the feasibility of their use in obstetrics and gynecology. *Acta Biomater.* **2019**, *97*, 623–636. [CrossRef]
5.  Wang, S.; Zhang, X.; Li, J.-A.; Liu, C.; Guan, S.; Wang, S.; Zhang, X.; Li, J.-A.; Liu, C.; Guan, S. Investigation of Mg-Zn-Y-Nd alloy for potential application of biodegradable esophageal stent material. *Bioact. Mater.* **2020**, *5*, 1–8. [CrossRef]
6.  Hwang, D.; Yang, S.; Zhang, J.; Koo, B.-K. Physiologic Assessment after Coronary Stent Implantation. *Korean Circ. J.* **2021**, *51*, 189–201. [CrossRef]
7.  Alaneme, K.K.; Kareem, S.A.; Olajide, J.L.; Sadiku, R.E.; Bodunrin, M.O. Computational biomechanical and biodegradation integrity assessment of Mg-based biomedical devices for cardiovascular and orthopedic applications: A review. *Int. J. Light. Mater. Manuf.* **2022**, *5*, 251–266. [CrossRef]
8.  Gu, X.; Cheng, J.; Li, L.; Ni, Z. Numerical simulation and experimental test of hemodynamics in vessel-stent coupling systems. *J. Southeast Univ.* **2012**, *6*, 1089–1093. (In Chinese) [CrossRef]
9.  Wei, Y.; Cheng, J. Hemodynamics Experimental Research of Stent Coupling System of Pulse Flow. *Life Sci. Instrum.* **2017**, *15*, 29–33. (In Chinese) [CrossRef]
10. Jiang, X.; Teng, X.; Shi, D.; Zhang, Y. Numerical simulation research on mechanical behavior of intervention coupling systems for coronary stents. *Eng. Mech.* **2016**, *33*, 231–237. [CrossRef]
11. Li, P.; Liu, Z.; Jiang, X.; Teng, X. Arterial Injury Assessment by Computational Interaction Model of Shear Thinning Blood with Expanded Stenotic Vascular. *J. Shanghai Jiaotong Univ.* **2019**, *53*, 757–764.
12. Song, K.; Bi, Y.; Zhao, H.; Wu, T.; Xu, F.; Zhao, G. Structural optimization and finite element analysis of poly- l -lactide acid coronary stent with improved radial strength and acute recoil rate. *J. Biomed. Mater. Res. Part B Appl. Biomater.* **2020**, *108*, 2754–2764. [CrossRef]
13. Melzer, H.-S.; Ahrens, R.; Guber, A.E.; Dohse, J. Numerical simulation and in vitro examination of the flow behaviour within coronary stents. *Curr. Dir. Biomed. Eng.* **2019**, *5*, 541–544. [CrossRef]
14. Ren, Q.; Li, Q.; Qiao, A. Mechanical Analyses of Stents with Different Structures under Compressing State. *Biophysics* **2014**, *2*, 15–22. [CrossRef]
15. Li, Z.; Feng, H. Coupling Deformation Mechanism for Coronary Stents with Different Materials. *Chin. J. Rare Met.* **2018**, *42*, 931–936.
16. Blair, R.W.; Dunne, N.J.; Lennon, A.B.; Menary, G.H. Multi-objective optimisation of material properties and strut geometry for poly(L-lactic acid) coronary stents using response surface methodology. *PLoS ONE* **2019**, *14*, e0218768. [CrossRef]
17. Toong, D.W.Y.; Ng, J.C.K.; Cui, F.; Leo, H.L.; Zhong, L.; Lian, S.S.; Venkatraman, S.; Tan, L.P.; Huang, Y.Y.; Ang, H.Y. Nanoparticles-reinforced poly-l-lactic acid composite materials as bioresorbable scaffold candidates for coronary stents: Insights from mechanical and finite element analysis. *J. Mech. Behav. Biomed. Mater.* **2021**, *125*, 104977. [CrossRef]
18. Melzer, H.-S.; Ahrens, R.; Guber, A.E.; Dohse, J. The influence of strut-connectors in coronary stents: A comparison of numerical simulations and μPIV measurements. *Curr. Dir. Biomed. Eng.* **2020**, *6*, 392–395. [CrossRef]
19. Chiastra, C.; Mazzi, V.; Rizzini, M.L.; Calò, K.; Corti, A.; Acquasanta, A.; De Nisco, G.; Belliggiano, D.; Cerrato, E.; Gallo, D.; et al. Coronary Artery Stenting Affects Wall Shear Stress Topological Skeleton. *J. Biomech. Eng.* **2022**, *144*, 061002. [CrossRef]
20. Lagache, M.; Coppel, R.; Finet, G.; Derimay, F.; Pettigrew, R.; Ohayon, J.; Malvè, M. Impact of Malapposed and Overlapping Stents on Hemodynamics: A 2D Parametric Computational Fluid Dynamics Study. *Mathematics* **2021**, *9*, 795. [CrossRef]
21. Xue, H.; Saha, S.C.; Beier, S.; Jepson, N.; Luo, Z. Topological Optimization of Auxetic Coronary Stents Considering Hemodynamics. *Front. Bioeng. Biotechnol.* **2021**, *9*, 728914. [CrossRef]
22. Razavi, S.E.; Farhangmehr, V.; Babaie, Z. Numerical investigation of hemodynamic performance of a stent in the main branch of a coronary artery bifurcation. *BioImpacts* **2019**, *9*, 97–103. [CrossRef]
23. Lan, Y.; Chen, F.; Cheng, Y.; Che, W.; Zhou, Y.; Lu, Y.; Wang, H.; Liu, Q.; Ng, E.Y.K.; Peng, Y.; et al. A Nine Months Follow-up Study of Hemodynamic Effect on Bioabsorbable Coronary Stent Implantation. *IEEE Access* **2019**, *7*, 112564–112571. [CrossRef]
24. Wei, L.; Leo, H.L.; Chen, Q.; Li, Z.-Y. Structural and Hemodynamic Analyses of Different Stent Structures in Curved and Stenotic Coronary Artery. *Front. Bioeng. Biotechnol.* **2019**, *7*, 366. [CrossRef]
25. Beier, S.; Ormiston, J.; Webster, M.; Cater, J.; Norris, S.; Medrano-Gracia, P.; Young, A.; Cowan, B. Hemodynamics in Idealized Stented Coronary Arteries: Important Stent Design Considerations. *Ann. Biomed. Eng.* **2015**, *44*, 315–329. [CrossRef]
26. Mohammed, A.M.; Ariane, M.; Alexiadis, A. Fluid-Structure Interaction in Coronary Stents: A Discrete Multiphysics Approach. *ChemEngineering* **2021**, *5*, 60. [CrossRef]
27. Xu, J.; Yang, J.; Huang, N.; Uhl, C.; Zhou, Y.; Liu, Y. Mechanical response of cardiovascular stents under vascular dynamic bending. *Biomed. Eng. Online* **2016**, *15*, 21. [CrossRef]

28. Barati, S.; Fatouraee, N.; Nabaei, M.; Berti, F.; Petrini, L.; Migliavacca, F.; Matas, J.F.R. A computational optimization study of a self-expandable transcatheter aortic valve. *Comput. Biol. Med.* **2021**, *139*, 104942. [CrossRef]

29. Mao, Y.; Li, Y.; Chen, Y.; Miao, Y.; Deng, Q.; Niu, W. Hyperelastic behavior of two rubber materials under quasistatic and dynamic compressive loadings—Testing, modeling and application. *Polimery* **2015**, *60*, 516–522. [CrossRef]

30. Kamangar, S. Numerical simulation of pulsatile blood flow characteristics in a multi stenosed coronary artery. *Bio-Med. Mater. Eng.* **2021**, *32*, 309–321. [CrossRef]

31. Onder, A.; Yapici, R.; Incebay, O. An experimental performance comparison of Newtonian and non-Newtonian fluids on a centrifugal blood pump. *Proc. Inst. Mech. Eng. Part H J. Eng. Med.* **2022**, *236*, 399–405. [CrossRef] [PubMed]

32. Liu, H.; Lan, L.; Abrigo, J.; Ip, H.L.; Soo, Y.; Zheng, D.; Wong, K.S.; Wang, D.; Shi, L.; Leung, T.W.; et al. Corrigendum: Comparison of Newtonian and Non-newtonian Fluid Models in Blood Flow Simulation in Patients With Intracranial Arterial Stenosis. *Front. Physiol.* **2021**, *12*, 782647. [CrossRef]

33. Chen, S.; Zhang, B.; Zhang, B.; Lin, H.; Yang, H.; Zheng, F.; Chen, M.; Ke, Y. Assessment of structure integrity, corrosion behavior and microstructure change of AZ31B stent in porcine coronary arteries. *J. Mater. Sci. Technol.* **2020**, *39*, 39–47. [CrossRef]

34. Cheng, G.C.; Loree, H.M.; Kamm, R.D.; Fishbein, M.C.; Lee, R.T. Distribution of circumferential stress in ruptured and stable atherosclerotic lesions. A structural analysis with histopathological correlation. *Circulation* **1993**, *87*, 1179–1187. [CrossRef] [PubMed]

35. Guzman, R.J. Clinical, cellular, and molecular aspects of arterial calcification. *J. Vasc. Surg.* **2007**, *45*, 57–63. [CrossRef]

36. Tomaszewski, M.; Sybilski, K.; Małachowski, J.; Wolański, W.; Buszman, P.P. Numerical and experimental analysis of balloon angioplasty impact on flow hemodynamics improvement. *Acta Bioeng. Biomech.* **2020**, *22*, 283–306. [CrossRef]

37. Tomaszewski, M.; Sybilski, K.; Baranowski, P.; Małachowski, J. Experimental and numerical flow analysis through arteries with stent using particle image velocimetry and computational fluid dynamics method. *Biocybern. Biomed. Eng.* **2020**, *40*, 740–751. [CrossRef]